A Concerted Enzymatic and Bioorthogonal Approach for Extra- and Intracellular Activation of Environment-Sensitive Ruthenium(II)-Based Imaging Probes and Photosensitizers

Shum, Justin; Lee, Lawrence Cho-Cheung; Chiang, Michael Wai-Lun; Lam, Yun-Wah; Lo, Kenneth Kam-Wing

Published in:
Angewandte Chemie (International Edition)

Published: 17/07/2023

Document Version:
Post-print, also known as Accepted Author Manuscript, Peer-reviewed or Author Final version

Published version (DOI):
10.1002/anie.202303931

Publication details:
Shum, J., Lee, L. C.-C., Chiang, M. W.-L., Lam, Y.-W., & Lo, K. K.-W. (2023). A Concerted Enzymatic and Bioorthogonal Approach for Extra- and Intracellular Activation of Environment-Sensitive Ruthenium(II)-Based Imaging Probes and Photosensitizers. *Angewandte Chemie (International Edition)*, *62*(29), Article e202303931. https://doi.org/10.1002/anie.202303931

A Journal of the Gesellschaft Deutscher Chemiker

Angewandte International Edition GDCh Chemie

www.angewandte.org

Accepted Article

Title: A Concerted Enzymatic and Bioorthogonal Approach for Extracellular and Intracellular Activation of Environment-Sensitive Ruthenium(II)-Based Imaging Probes and Photosensitizers

Authors: Justin Shum, Lawrence Cho-Cheung Lee, Michael Wai-Lun Chiang, Yun Wah Lam, and Kenneth Kam-Wing Lo

To be cited as: *Angew. Chem. Int. Ed.* **2023**, e202303931

Link to VoR: https://doi.org/10.1002/anie.202303931

WILEY VCH

10.1002/anie.202303931

WILEY-VCH

RESEARCH ARTICLE

A Concerted Enzymatic and Bioorthogonal Approach for Extracellular and Intracellular Activation of Environment-Sensitive Ruthenium(II)-Based Imaging Probes and Photosensitizers

Justin Shum,[a] Lawrence Cho-Cheung Lee,[a, b] Michael Wai-Lun Chiang,[a] Yun-Wah Lam,[a] and Kenneth Kam-Wing Lo*[a, c]

[a] J. Shum, Dr. L. C.-C. Lee, M. W.-L. Chiang, Dr. Y.-W. Lam, Prof. K. K.-W. Lo
Department of Chemistry
City University of Hong Kong
Tat Chee Avenue, Kowloon, Hong Kong, P. R. China
E-mail:bhkenlo@cityu.edu.hk
[b] Dr. L. C.-C. Lee
Laboratory for Synthetic Chemistry and Chemical Biology Limited
Units 1503-1511, 15/F, Building 17 W, Hong Kong Science Park, New Territories, Hong Kong, P. R. China
[c] Prof. K. K.-W. Lo
State Key Laboratory of Terahertz and Millimeter Waves
City University of Hong Kong
Tat Chee Avenue, Kowloon, Hong Kong, P. R. China

Supporting information for this article is given via a link at the end of the document.

Abstract: In this article, we report a novel targeting strategy involving the combination of an enzyme-instructed self-assembly (EISA) moiety and a strained cycloalkyne to generate large accumulation of bioorthogonal sites in cancer cells. These bioorthogonal sites can serve as activation triggers in different regions for transition metal-based probes, which are new ruthenium(II) complexes carrying a tetrazine unit for controllable phosphorescence and singlet oxygen generation. Importantly, the environment-sensitive emission of the complexes can be further enhanced in the hydrophobic regions offered by the large supramolecular assemblies, which is highly advantageous to biological imaging. Additionally, the (photo)cytotoxicity of the large supramolecular assemblies containing the complexes was investigated, and the results illustrate that cellular localization (extracellular and intracellular) imposes a profound impact on the efficiencies of photosensitizers.

Introduction

Photodynamic therapy (PDT) is a useful therapeutic modality for cancer treatment utilizing photosensitizers (PSs) that, upon specific light irradiation, generate cytotoxic reactive oxygen species (ROS).[1] This minimally invasive therapeutic approach has led to the development of many elegant PSs that have been clinically approved,[2] however most are based on metal-containing tetrapyrrolic scaffolds. Many of these PSs suffer from low water solubility, and photobleaching hampers their efficiency as PDT agents. Another major limitation is that many cancer patients experience photosensitivity due to the nonselective distribution of the PSs and the uncontrollable generation of cytotoxic ROS (“always on” PSs). One of the major efforts to circumvent photosensitivity is to develop activatable PSs responsive to the tumor microenvironment (e.g., low pH and high glutathione (GSH) level),[3] but the sensitivity is still not satisfactory since the lysosomes of normal cells are also highly acidic, and the cytoplasmic concentration of GSH is within the millimolar range. Thus, there is a critical need for selective targeting and accumulation of PDT agents in cancer cells. Recent progress in enzyme-instructed self-assembly (EISA) has demonstrated that enzymatic cleavage of small molecular motifs appended with an enzyme substrate can lead to the formation of well-defined supramolecular assemblies in cancer cells.[4] The overexpression of specific enzymes in cancer cells compared to normal cells allows for selective diagnostic and therapeutic applications. Many of these EISA examples utilize the overexpressed alkaline phosphatase (ALP) in cancer cells, a commonly tested cancer biomarker in clinical settings,[5] to selectively induce enzyme sequestration,[6] suppression of cell migration,[7] and cell death of cancer cells.[8] Recently, a new two-step strategy incorporating EISA with bioorthogonal reporters has allowed novel selective prodrug activation.[9] A two-step approach is favorable to balance the efficacy and safety of anticancer drugs. The combination of EISA and bioorthogonal chemistry elicits spatiotemporal targeting and accumulation in cancer cells and the selective generation of highly cytotoxic anticancer agents, respectively.

We propose that a two-step EISA and bioorthogonal approach is a promising strategy for the accumulation and activation of PSs (Figure 1). The coupling of a bioorthogonal group to a self-assembling motif facilities the selective targeting of cancer cells with overexpressed enzymes and large accumulation of bioorthogonal sites via EISA. We chose to use ruthenium(II) polypyridine complexes as the bioorthogonal reaction partner due to various advantages: 1) octahedral geometry could modulate the dimensionality of intermolecular interactions of the supramolecular assemblies to form unique well-defined structures,[10] 2) excellent water solubility suitable for biological applications; 3) triplet metal-to-ligand charge transfer (^{3}MLCT) emission with high environment sensitivity, 4) efficient PSs for PDT, and 5) controllable phosphorescence and singlet oxygen ($^1O_2$) generation via bioorthogonal reaction.[11] Previous

10.1002/anie.202303931

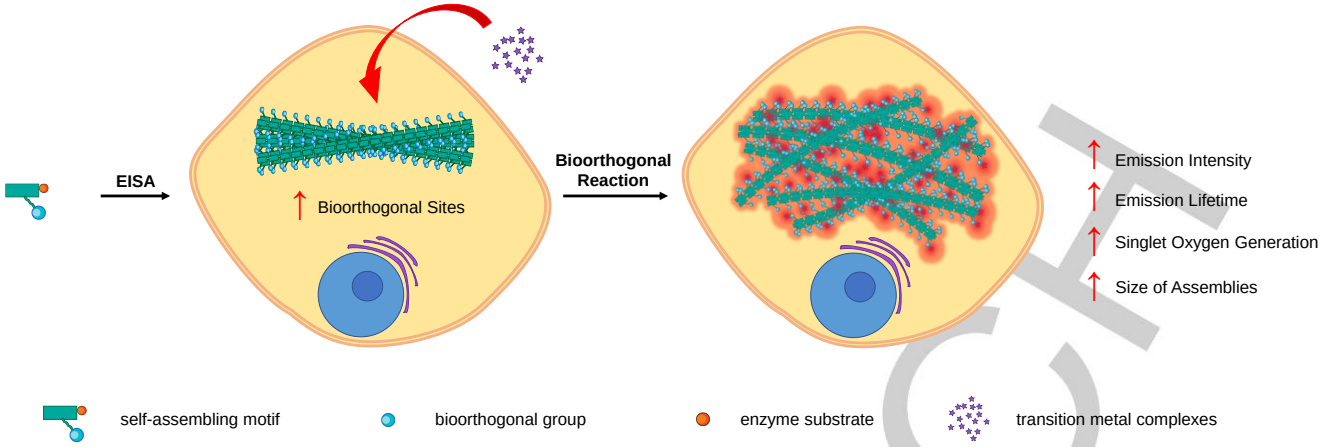

Figure 1. Schematic illustration of EISA of small self-assembling motifs to generate large supramolecular assemblies with many bioorthogonal sites and upon bioorthogonal reaction leads to greatly enhanced emission intensity, lifetime extension, and singlet oxygen generation.

work on metal complexes and their environment-sensitive emission has demonstrated that more pronounced emission enhancement and extended emission lifetimes can be achieved if they are located in a hydrophobic environment.[12] Thus, we anticipate that the supramolecular assemblies will provide hydrophobic regions to elicit further emission enhancement and lifetime extension even when the emission is already turned on after the bioorthogonal reaction. Notably, this strategy offers versatile interchanging of bioorthogonal reaction partners as an adaptation to target other overexpressed hallmarks of cancer.

Results and Discussion

Design of the Ruthenium(II) Tetrazine Complexes

Our previous studies on the inverse electron-demand Diels–Alder (IEDDA) reaction of transition metal–tetrazine complexes with (1*R*,8*S*,9*s*)-bicyclo[6.1.0]nonyne (BCN) derivatives show that the direct coordination of a tetrazine ligand to the metal center can significantly accelerate the IEDDA reaction kinetics due to the cationic metal center.[13] Additionally, this design can effectively suppress the $^1O_2$ generation efficiency of the tetrazine complexes, preventing unwanted photocytotoxicity.[13b] Thus, in this work, we selected 6-phenyl-3-(2-pyridyl)tetrazine (py-tz-ph) as a coordinating diimine ligand for the synthesis of three ruthenium(II) pyridyl-tetrazine complexes: $[Ru(N^N)_2(py\text{-}tz\text{-}ph)](Cl)_2$ (N^N = 2,2'-bipyridine (bpy) (**1**), 4,7-diphenyl-1,10-phenanthroline (Ph_2-phen) (**2**), and 2,2'-biquinoline (biq) (**3**)) (Scheme 1). Remarkably, complex **3** was designed as an NIR-emitting phosphorogenic probe by using two strong π-accepting biq ligands. All the complexes were obtained as Cl^- salts and displayed good water solubility (≥ 5 mM) at room temperature. The IEDDA reaction products (**1-BCN** – **3-BCN**, Scheme 1) were also synthesized from the reaction of complexes **1** – **3** with (1*R*,8*S*,9*s*)-bicyclo[6.1.0]non-4-yn-9-ylmethanol (BCN-OH) in methanol, and isolated as Cl^- salts for comparison studies. Detailed synthetic procedures and characterization data (^1H and ^{13}C NMR, ESI-MS, and HR-MS) of the ruthenium(II) complexes are included in the Supporting Information.

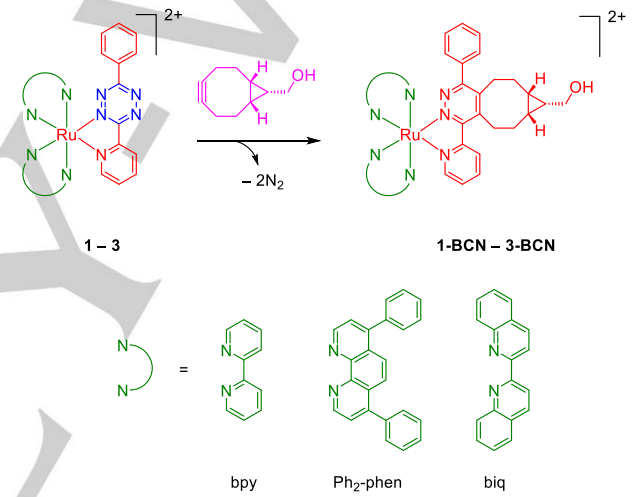

Scheme 1. Structures of the ruthenium(II) pyridyl-tetrazine complexes **1** – **3** and pyridazine complexes **1-BCN** – **3-BCN**.

Photophysical and Photosensitization Behavior

We first examined the photophysical properties of the ruthenium(II) tetrazine complexes **1** – **3** and pyridazine complexes **1-BCN** – **3-BCN**. Both the bpy complexes (**1** and **1-BCN**) and Ph_2-phen complexes (**2** and **2-BCN**) showed intense absorption bands at 250 – 350 nm, which are attributed to spin-allowed intraligand (^{1}IL) (π → π*) (N^N) (Table S1 and Figure S1). The weaker absorption bands of the tetrazine complexes (**1** and **2**) at 450 – 600 nm and pyridazine complexes (**1-BCN** and **2-BCN**) at 400 – 550 nm are assigned to spin-allowed metal-to-ligand charge transfer (^{1}MLCT) (dπ(Ru) → π*(N^N)) transitions.[14] The tetrazine complex **3** and its pyridazine counterpart **3-BCN** displayed similar intense ^{1}IL (π → π*) (N^N) absorption features in the UV region (*ca.* 250 – 400 nm) and weaker ^{1}MLCT (dπ(Ru) → π*(N^N)) transitions at 450 – 650 nm (Table S1 and Figure S1).[15] The tetrazine absorption due to the (*n* → π*) (py-tz-ph) transition of complexes **1** – **3** should be embedded in the lower energy ^{1}MLCT

10.1002/anie.202303931

absorption features. Upon photoexcitation, all the complexes exhibited orange to red emission in solutions under ambient conditions and in low-temperature alcohol glass (Table S2). Their emission maxima displayed significant blue shifts upon cooling the samples to 77 K, indicative of spin-forbidden ^{3}MLCT (dπ(Ru) → π*(N^N)) character.[15b,16] Importantly, the tetrazine complexes **1** – **3** displayed extremely weak red or NIR emission (Φ_{em} = 0.0003 – 0.0017; Table S2) in fluid solutions, indicative of efficient quenching by the tetrazine unit.[13] In contrast, the pyridazine complexes **1-BCN** – **3-BCN** showed more intense and longer-lived emission (Φ_{em} = 0.0011 – 0.023, τ_o = 0.08 – 0.24 μs; Table S2) in fluid solutions. The $^1O_2$ generation efficiencies of all the complexes were evaluated by monitoring the $^1O_2$ emission centered at *ca.* 1276 nm. The tetrazine complexes **1** – **3** displayed low $^1O_2$ generation yields (Φ_Δ = 0.02 – 0.19; Table S3), which should result from the strong quenching capability of the tetrazine unit.[17] In contrast, the pyridazine complexes **1-BCN** – **3-BCN** displayed higher $^1O_2$ generation efficiencies (Φ_Δ = 0.19 – 0.66; Table S3), demonstrating the controllable $^1O_2$-photosensitization properties of the ruthenium(II) complexes via the IEDDA reaction.

Bioorthogonal Reactivity

Bioorthogonal reactions with fast reaction rates are favorable to ensure unreacted probes are at a minimal (higher signal-to-noise ratios) and allow simple translation to animal models.[18] The bioorthogonal reactivity of the tetrazine complexes **1** – **3** was investigated with BCN-OH as a model substrate in water/MeOH (1:1, *v*/*v*) at 298 K by monitoring the emission of the complexes. The second-order rate constants (k_2) for the reaction of the complexes with BCN-OH were determined to be 11.4 – 1550 M^{-1} s^{-1} (Table 1), with complex **3** exhibiting the fastest reaction rates. The accelerated reaction kinetics of complexes **2** and **3** should result from the stronger π-accepting diimine ligands, Ph_2-phen and biq. The phosphorogenic response of complexes **1** – **3** toward BCN-OH was also studied. The addition of BCN-OH to the solution of complexes led to substantial emission enhancement and lifetime extension (I/I_o = 3.4 – 28.3, τ = 0.22 – 0.31 μs; Table 1) due to the conversion of the quenching tetrazine unit to a non-quenching pyridazine moiety. These remarkable properties highlight the advantage of metal-based bioorthogonal photosensitizers for controllable phosphorescence and $^1O_2$ generation.

Table 1. Second-order rate constants (k_2) for the reactions of the ruthenium(II) tetrazine complexes **1** – **3** with BCN-OH in water/MeOH (1:1, *v*/*v*) at 298 K. Emission enhancement factors (I/I_o) and lifetimes (τ) of the ruthenium(II) tetrazine complexes **1** – **3** (20 μM) upon incubation with BCN-OH (200 μM) in aerated water/DMSO (99:1, *v*/*v*) at 298 K for 24 h.

Complex	k_2 [M^{-1} s^{-1}]	I/I_o[a]	τ [μs][b]
1	11.4 ± 1.0	5.4	0.26
2	32.8 ± 8.9	28.3	0.31
3	1550 ± 43	3.4	0.22

[a] I_o and I are the emission intensities of the complexes in the absence and presence of BCN-OH.

[b] The lifetimes were measured at the emission maxima of the products **1-BCN** – **3-BCN** (λ_{ex} = 355 nm).

Design of Self-Assembly Motif

Our design of the self-assembly motif focuses on a known EISA motif (Nap-FFKYp (P1))[19] and its BCN-modified version (Nap-FFK(BCN)Yp (FFBCN1)) (Figure 2), which was obtained by attaching a hydrophobic cyclooctyne moiety to the lysine residue of P1. A dephosphorylated analog, Nap-FFK(BCN)Y (FFBCN2), was also synthesized for comparison studies. The naphthalene (Nap) group at the N-terminus and the aromatic groups of the FF backbone are important to the self-assembly behavior of the peptides by facilitating aromatic-aromatic interactions.[20] The presence of a phosphate group in FFBCN1 can not only endow the peptide with ALP-responsive character but also increase the water solubility of the peptide. As such, the dephosphorylation of the peptide FFBCN1 is expected to effectively promote the self-assembly of the resultant product FFBCN2 via π–π and hydrophobic interactions.

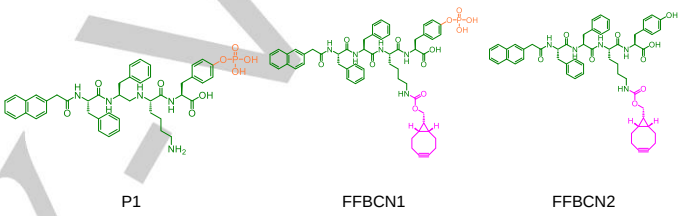

Figure 2. Structures of peptides P1, FFBCN1, and FFBCN2.

Enzyme Instructed Self-Assembly Ability

The critical micelle concentrations (CMCs) of the peptides were first determined to assess the minimal concentration for nanofiber formation. The CMCs of P1, FFBCN1, and FFBCN2 were determined to be 211, 25.4, and 11.6 μM, respectively (Figure 3A). Interestingly, the modification of P1 with a BCN unit significantly decreased the CMC by *ca*. 8-fold, indicating that the attachment of the BCN moiety would enhance the self-assembling ability of the peptide. The CMC of FFBCN2 is lower than that of FFBCN1 due to the presence of a hydroxyl group instead of a highly ionic phosphate group on the tyrosine residue. Next, the self-assembly behavior of FFBCN1 was investigated *in vitro* at 200 μM using transmission electron microscopy (TEM). Only amorphous micellular shapes were observed in the absence of ALP (Figure 3B, left). Upon ALP-catalyzed dephosphorylation, FFBCN1 was converted to FFBCN2, as evidenced by ESI-MS (Figure S2), forming short nanofibers with a width of 27.9 ± 6 nm (Figure 3B, right). In the absence of ALP, FFBCN2 only formed short nanofibers with a width of 24.0 ± 6.8 (Figure S3). Dynamic light scattering (DLS) studies further confirmed that dephosphorylation of FFBCN1 resulted in a substantial increase in the average particle size from 18.17 to 295.3 nm (Figure 3C), which should be a result of the self-assembly of the peptide to form short nanofibers. The dephosphorylation of FFBCN1 by ALP in water/DMSO (99:1, *v*/*v*) at different time points was monitored by HPLC. As shown in Figure 3D, FFBCN1 was fully converted to FFBCN2 after *ca*. 16 h. The combined results demonstrate that modification of the EISA motif P1 with a BCN unit can significantly enhance the self-assembly behavior of the peptide without affecting the dephosphorylation activity of the ALP enzyme.

10.1002/anie.202303931

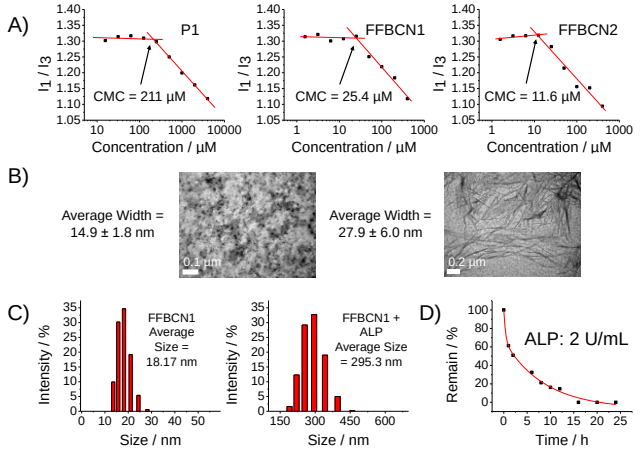

Figure 3. A) The CMCs of P1 (left), FFBCN1 (middle), and FFBCN2 (right) in water/DMSO (99:1, *v*/*v*). B) TEM images of FFBCN1 (200 μM) without ALP (left) or with ALP (2 U mL^{-1}, 24 h; right) in water/DMSO (99:1, *v*/*v*). C) Size distribution of FFBCN1 (200 μM) without ALP (left) or with ALP (2 U mL^{-1}, 24 h; right) in water/DMSO (99:1, *v*/*v*). D) Dephosphorylation of FFBCN1 (200 μM) by ALP in water/DMSO (99:1, *v*/*v*) at different time points, monitored by HPLC.

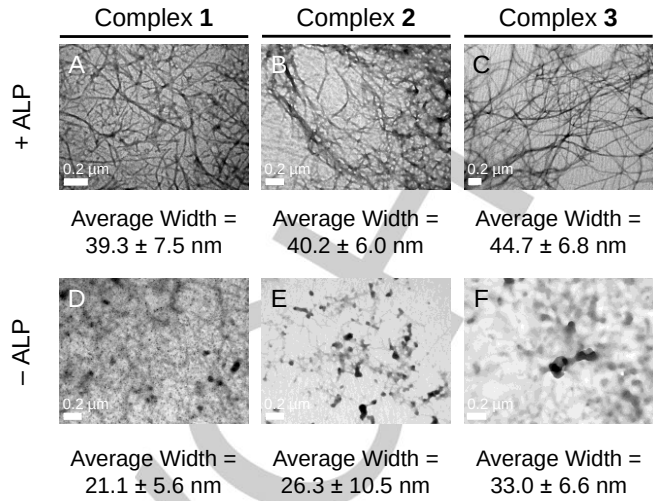

Figure 4. TEM images of FFBCN1 (200 μM) pretreated with ALP (2 U mL^{-1}, 24 h) (A – C) or in the absence of ALP (D – F) and further incubated with complex **1** (20 μM, 4 h; A, D), complex **2** (20 μM, 4 h; B, E), and complex **3** (20 μM, 4 h; C, F) in water/DMSO (99:1, *v*/*v*) at 37°C.

Concerted Enzymatic and Bioorthogonal Reactions

We then investigated the morphological changes of the short nanofibers (resulting from the dephosphorylation of FFBCN1 by ALP) upon the IEDDA reaction with the tetrazine complexes. As revealed by TEM, incubation of the ALP-treated FFBCN1 with complexes **1** – **3** led to a change in the morphology from short nanofibers to a web-like structure with a width of 39.3 – 44.7 nm (Figure 4). The structural transformation was also evidenced by DLS analysis, which showed a significant increase in the average particle size from 295.3 nm to 615.1 – 1484 nm (Figure S4C). In contrast, incubation of FFBCN1 with complexes **1** – **3** in the absence of ALP only led to the formation of small micelles (Figure 4) with an average particle size of 15.7 – 24.4 nm (Figure S4B), indicating that the self-assembly behavior does not arise from the bioorthogonal reaction of FFBCN1 with the complexes. Additionally, the complexes alone formed small spherical aggregates (Figure S5) with an average particle size of 2.0 – 3.6 nm (Figure S4A), revealing that the complexes do not possess any self-assembly properties and merely exist as small spherical particles. The phosphorogenic response of complexes **1** – **3** toward the BCN-modified peptide FFBCN1 and the resultant supramolecular assemblies were also studied. Incubation of the complexes with FFBCN1 led to substantial emission enhancement and lifetime extension (I/I_0 = 7.0 – 89.9, τ = 0.34 – 0.59 μs; Table 2 and Figure 5), which are higher and longer than those with BCN-OH (I/I_0 = 3.4 – 28.3, τ = 0.22 – 0.31 μs; Table 1 and Figure 5). Importantly, treatment of FFBCN1 with ALP prior to the addition to the tetrazine complexes resulted in an even more significant increase in the emission intensities and lifetimes (I/I_0 = 12.4 – 109.9, τ = 0.38 – 0.66 μs; Table 2 and Figure 5), which should be associated with the highly hydrophobic and rigid local environment offered by the nanostructures formed from the

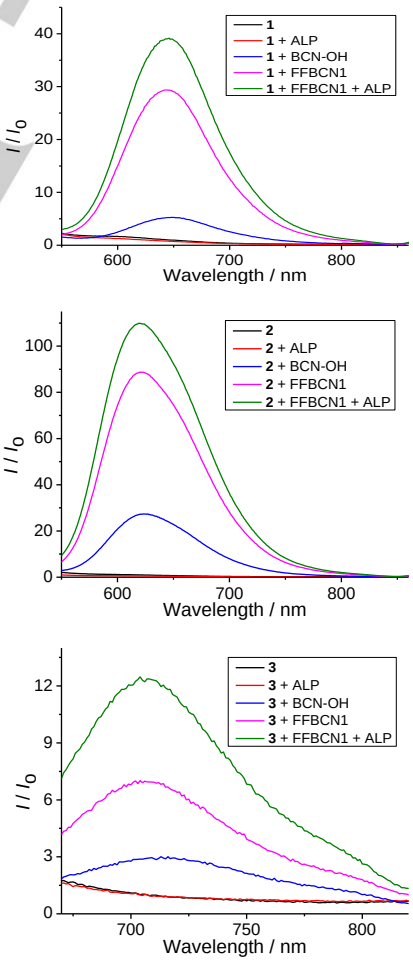

Figure 5. Emission spectra of the ruthenium(II) tetrazine complexes **1** (top), **2** (middle), and **3** (bottom) (20 μM) in the absence (black) and presence of ALP (2 U mL^{-1}; red), BCN-OH (200 μM; blue), FFBCN1 (200 μM; magenta), and FFBCN1 (200 μM) + ALP (2 U mL^{-1}) (green) in water/DMSO (99:1, *v*/*v*) at 298 K for 24 h. λ_{ex} = 450 nm.

10.1002/anie.202303931

Table 2. Emission enhancement factors (I/I_o) and lifetimes (τ) of the ruthenium(II) tetrazine complexes **1** – **3** (20 μM) upon incubation with FFBCN1 (200 μM), FFBCN1 (200 μM) + ALP (2 U mL^{-1}), or ALP (2 U mL^{-1}) in water/DMSO (99:1, *v*/*v*) at 298 K for 24 h.

	FFBCN1		FFBCN1 + ALP		ALP	
Complex	I/I_o[a]	τ [μs][b]	I/I_o[a]	τ [μs][b]	I/I_o[a]	τ [μs][b]
1	28.3	0.50	39.2	0.55	0.8	—[c]
2	89.9	0.59	109.9	0.66	0.7	—[c]
3	7.0	0.34	12.4	0.38	1.0	—[c]

[a] I_o and I are the emission intensities of the complexes in the absence and presence of the dienophiles or enzyme, respectively.

[b] The lifetimes were measured at the emission maxima (λ_{ex} = 355 nm).

[c] Could not be determined with accuracy due to very weak emission.

dephosphorylation of FFBCN1. No similar emission enhancement was observed upon incubation of the complexes with ALP only, indicating that the emission "turn-on" resulted from the bioorthogonal ligation with the BCN unit on the supramolecular assemblies rather than nonspecific interactions with the enzyme. These results collectively show that our proposed two-step EISA-based bioorthogonal activation strategy can rapidly generate luminescent supramolecular assemblies with environment-sensitive emission in ALP-overexpressing cancer cells for imaging applications.

Localization of Self-Assemblies in Live Cells

The cellular localization of the luminescent supramolecular assemblies formed from the EISA of FFBCN1 and the IEDDA reaction with the tetrazine complexes was examined by laser-scanning confocal microscopy (LSCM). We selected HeLa cells as a model cell line due to their high ALP expression level.[21] Complex **3** was used as a model compound in view of its favorable NIR emission and extremely fast reaction kinetics, as well as the large, well-defined nanostructures formed upon the IEDDA reaction. The cells were treated with FFBCN1 at concentrations ranging from 25 to 200 μM for 16 h, washed thoroughly with PBS (1 mL × 3), and incubated with complex **3** (20 μM, 4 h). Serendipitously, the localization of the luminescent supramolecular assemblies varied based on the concentration of FFBCN1 (Figure 6). At a high FFBCN1 concentration (200 μM), strong emission was mainly detected on the plasma membrane of the HeLa cells; yet at lower concentrations (≤ 100 μM), the emission was detected in the intracellular region of the cells. Notably, small-to-large vesicle structures (Figure S6) were observed inside the cells, indicative of the intracellular EISA of FFBCN1 at low concentrations. In light of this result, the EISA behavior of FFBCN1 at 100 μM was investigated with TEM (Figure S7) and DLS (Figure S8). The peptide would self-assemble into short nanofibers with a width of 21.1 ± 5.0 nm (Figure S7B) and an average particle size of 127 nm (Figure S8A, right) in the presence of ALP. The morphology changed to web-like structures with a width of 18.8 ± 5.1 – 33.0 ± 6.9 nm (Figures S7C – E) and an average particle size of 204.6 – 631.4 nm (Figure S8C) upon IEDDA reaction with complexes **1** – **3**. The extracellular and intracellular formation of the nanofibers in HeLa cells at 200 and 100 μM concentrations of FFBCN1, respectively, was examined by TEM and scanning electron microscopy (SEM) (Figure 7). TEM images of cross-sectioned HeLa cells treated with FFBCN1 (200 μM, 16 h) only (Figure 7F) or complex **3** (20 μM, 4 h) only (Figure 7B), or a combination of both FFBCN1 (200 μM, 16 h) and complex **3** (20 μM, 4 h) (Figure 7G) showed similar morphology to healthy and untreated HeLa cells (Figure 7A) with a smooth and well-defined cell membrane. However, when the cells were incubated with FFBCN1 at 100 μM for 16 h (Figure 7C), a few large holes were visible in the cytoplasmic region of the cell. The holes were further exacerbated upon incubation of the FFBCN1-treated cells with complex **3** (20 μM, 4 h), with the cytoplasmic region containing many small-to-large holes (Figures 7D and 7E). The combined EISA and bioorthogonal treatment led to much larger supramolecular assemblies, agreeing with the TEM (Figure S7) and DLS experiments (Figure S8). As a complement, SEM was utilized to examine the effect of the concentrations of FFBCN1 on the surface of HeLa cells (Figure 8). Examination of HeLa cells without or with treatment with complex **3** only (20 μM, 4 h) showed that the cells were covered in microvilli and membrane vesicles (Figures 7A and 7B), demonstrating that the complex alone did not significantly influence the cellular membrane dynamics. HeLa cells treated with FFBCN1 (100 μM, 16 h) (Figure 8C) or FFBCN1 (100 μM, 16 h) and then complex **3** (20 μM, 4 h) (Figure 8D) showed a generally smooth topology with greatly reduced numbers of microvilli and membrane vesicles. Large bundles of nanofibers were observed on the surface of HeLa cells that were treated with a high concentration of FFBCN1 (200 μM, 16 h) (Figure 8E) and FFBCN1 (200 μM, 16 h) and then complex **3** (20 μM, 4 h) (Figure 8G). Notably, the order of treatment of the biorthogonal groups is critical, and the FFBCN1 peptide is the determining factor of the cellular localization of the ruthenium(II) complexes due to the large accumulation of multiple bioorthogonal reaction sites born from the EISA process and the fast IEDDA reaction rates of complex **3**. Additional incubation studies were carried out by reversing the incubation order of the biorthogonal reactants (Figure S9). In these experiments, HeLa cells were pretreated with complex **3** (20 μM, 4 h), washed thoroughly with PBS (1 mL × 3), and subsequently incubated with FFBCN1 (200 μM, 16 h). The absence of emission in the extracellular or intracellular region indicates that the internalized complex **3** and FFBCN1 did not undergo any IEDDA ligation due to a difference in their localization, further supplementing that the EISA activity of FFBCN1 dictates the localization of the ruthenium(II) complexes.

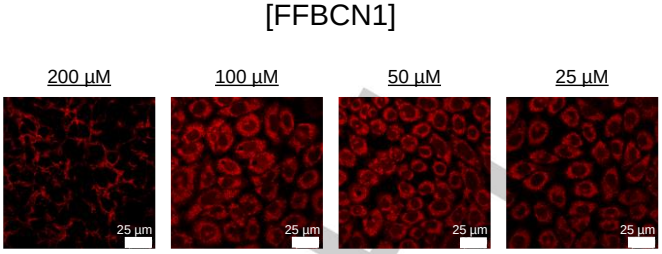

Figure 6. LSCM images of HeLa cells pretreated with FFBCN1 (25 – 200 μM, 16 h) and further incubated with complex **3** (20 μM, 4 h, λ_{ex} = 405 nm, and λ_{em} = 700 – 800 nm).

10.1002/anie.202303931

Colocalization studies with a high concentration of FFBCN1 (200 µM, 16 h), complex **3** (20 µM, 4 h), and CellMask Deep Red (5 µg mL^{-1}, 10 min) conferred sharp plasma membrane staining with a Pearson's correlation coefficient (PCC) of 0.90 (Figure 9A). In the low concentration condition, HeLa cells treated with FFBCN1 (100 µM, 16 h) and complex **3** (20 µM, 4 h) were costained with commercially available dyes for mitochondria (MitoTracker Deep Red FM, 100 nM, 30 min) and endoplasmic reticulum (ER-Tracker Red, 1 µM, 30 min), respectively (Figure 9B). After intracellular EISA and labeling of the nanofibers via IEDDA with complex **3**, the complex showed relatively good costain with MitoTracker Deep Red FM (PCC = 0.84) and moderate agreement with ER-Tracker Red (PCC = 0.66). Localization studies in normal human embryonic kidney cells (HEK293) that show low-level ALP expression were investigated to examine the selectivity of this strategy (Figure S10). Treatment of HEK293 cells with a low or high concentration of FFBCN1 and complex **3** demonstrated that the EISA self-assemblies could not form and only extremely weak emission could be observed, which should only result from the IEDDA reaction between FFBCN1 and complex **3**. These findings demonstrate that 1) the concentration of the small assembling motif is an important factor for EISA and could directly impact the cellular localization of the resulting supramolecular assemblies, and 2) ALP expression is crucial to forming the EISA self-assemblies. Notably, the combination of EISA and bioorthogonal chemistry is a promising strategy since the EISA of FFBCN1 allows the accumulation of many bioorthogonal sites for extracellular or intracellular applications that can be further selectively labeled with a complementary bioorthogonal probe.

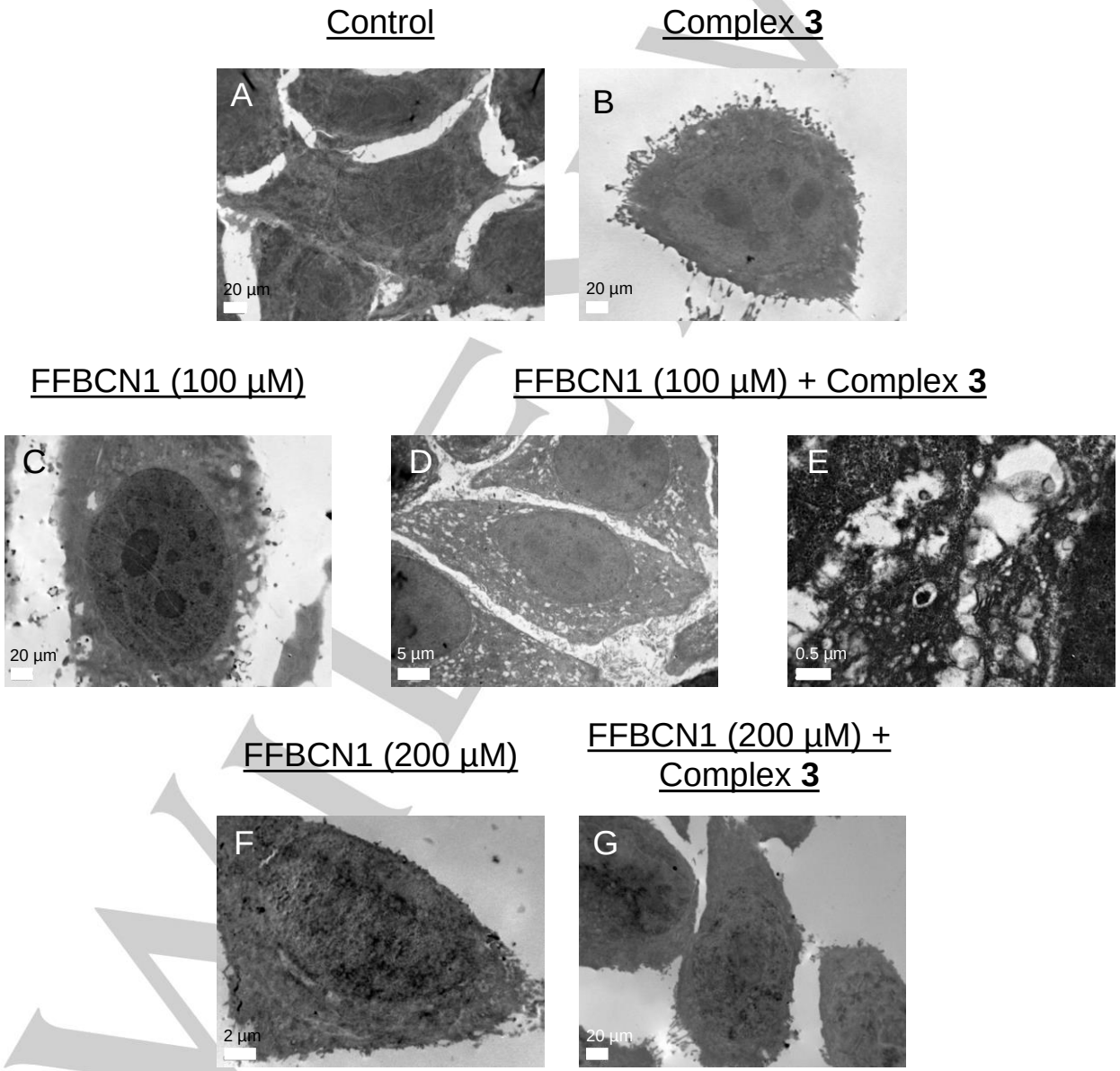

Figure 7. TEM images of A) untreated HeLa cells, B) HeLa cells treated with complex **3** (20 µM, 4 h), C) HeLa cells treated with FFBCN1 (100 µM, 16 h), D and E) HeLa cells pretreated with FFBCN1 (100 µM, 16 h) and further incubated with complex **3** (20 µM, 4 h), F) HeLa cells treated with FFBCN1 (200 µM, 16 h), and G) HeLa cells pretreated with FFBCN1 (200 µM, 16 h) and further incubated with complex **3** (20 µM, 4 h).

10.1002/anie.202303931

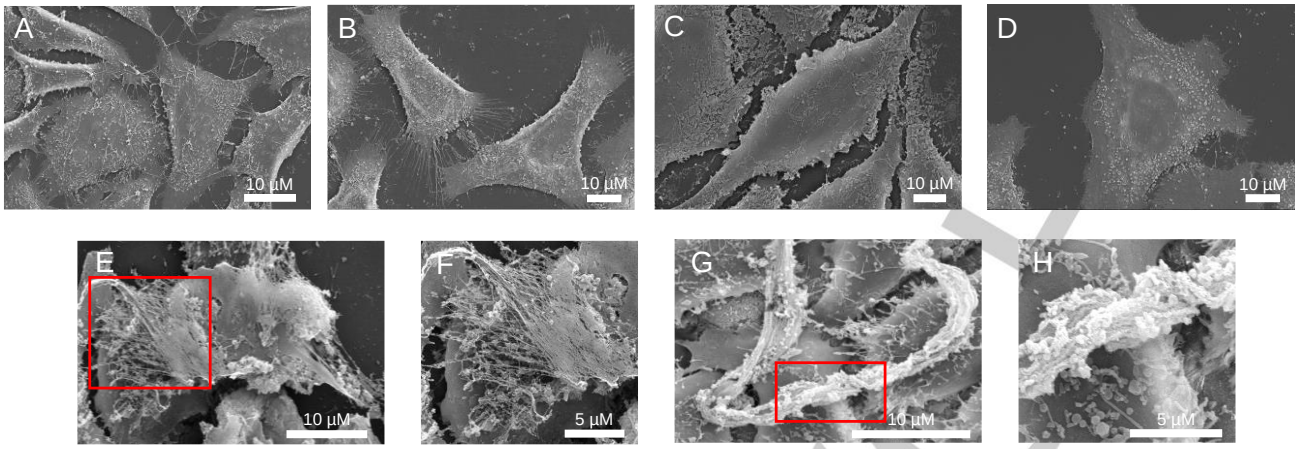

Figure 8. SEM images of A) untreated HeLa cells, B) HeLa cells treated with complex **3** (20 µM, 4 h), C) HeLa cells treated with FFBCN1 (100 µM, 16 h), D) HeLa cells pretreated with FFBCN1 (100 µM, 16 h) and further incubated with complex **3** (20 µM, 4 h), E) HeLa cells treated with FFBCN1 (200 µM, 16 h), F) magnified image of E, G) HeLa cells pretreated with FFBCN1 (200 µM, 16 h) and further incubated with complex **3** (20 µM, 4 h), and H) magnified image of G.

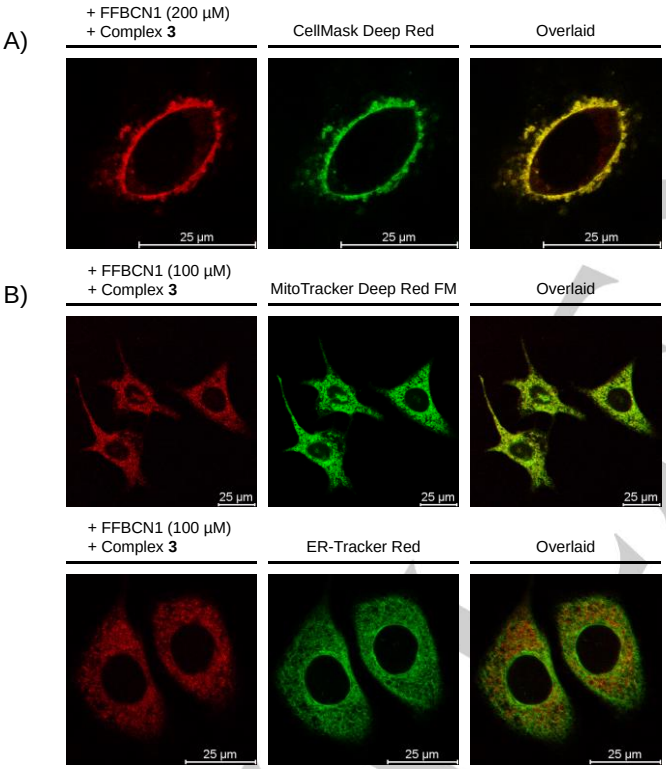

Figure 9. LSCM images of HeLa cells pretreated with A) FFBCN1 (200 µM, 16 h), further incubated with complex **3** (20 µM, 4 h, λ_{ex} = 405 nm, and λ_{em} = 700 – 800 nm), and subsequently incubated with CellMask Deep Red (5 µg mL^{-1}, 10 min, λ_{ex} = 649 nm, λ_{em} = 660 – 680 nm) (PCC = 0.90); B) FFBCN1 (100 µM, 16 h), further incubated with complex **3** (20 µM, 4 h, λ_{ex} = 405 nm, and λ_{em} = 700 – 800 nm), and subsequently incubated with MitoTracker Deep Red FM (100 nM, 30 min, λ_{ex} = 644 nm, λ_{em} = 660 – 680 nm) (PCC = 0.84) (upper) or ER-Tracker Red (1 µM, 30 min, λ_{ex} = 587 nm, λ_{em} = 610 – 630 nm) (PCC = 0.66) (lower).

Inhibition Studies

To further elucidate that the EISA process stems from the dephosphorylation of FFBCN1 and the major ALP enzymes in play, inhibition studies were carried out with phospholipase C (PLC),[22] 2,5-dimethoxy-N-(quinolin-3-yl)benzenesulfonamide (DQB),[23] and methyl-β-cyclodextrin (MβCD).[24,25] The enzyme PLC cleaves glycosylphosphatidylinositol anchors and removes ALP from the cell membrane.[22] DQB is a highly selective inhibitor of tissue-non-specific ALP (TNSALP) with no inhibitory activity toward placental alkaline phosphatases (PALP).[23] MβCD is a disruptor of ALP-rich lipid rafts[24] and caveolin endocytosis inhibitor.[25] Pretreatment of HeLa cells with PLC, DQB, or MβCD led to a substantial decrease in the emission intensity in cells treated with both high and low-concentration self-assemblies of FFBCN1 (Figure 10). These findings indicate that the EISA process cannot occur, and the extremely weak emission observed should only originate from the IEDDA reaction of FFBCN1 and complex **3**. These results agree that EISA is concentration- and reaction rate-dependent, and changes to the concentration could affect the self-assembly kinetics,[26] thus further impacting the cellular localization of the supramolecular assemblies. Our interpretation is shown in Figure 11. At a high concentration of FFBCN1 (200 µM), the major phosphatases for dephosphorylation of FFBCN1 are most likely PALP and some TNSALP. The PALP enzymes are mainly overexpressed in HeLa cells[27] and exist as membrane-bound and secretory forms. The large substrate concentration of FFBCN1 (200 µM) increases the enzymatic dephosphorylation rate, leading to an increased concentration of FFBCN2 and its rapid self-assembly, thus favoring self-assembly and accumulation on the plasma membrane rather than endocytosis. Treatment of HeLa cells with a lower concentration of FFBCN1 (100 µM) would favor endocytosis due to the lower concentration of FFBCN2 and the EISA of FFBCN1 occurring on the plasma membrane (PALP and TNSALP) and inside (e.g., phosphatases in endosomes)[28] the HeLa cells (Figure 11).

10.1002/anie.202303931
WILEY-VCH

RESEARCH ARTICLE

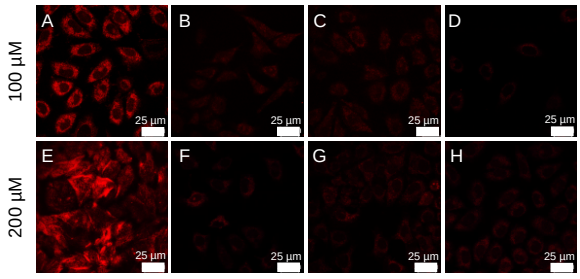

Figure 10. LSCM images of HeLa cells with: A) treatment of FFBCN1 (100 µM, 16 h) and further incubated with complex **3** (20 µM, 4 h, λ_{ex} = 405 nm, and λ_{em} = 700 – 800 nm); pretreatment with: B) PLC (0.2 U mL^{-1}, 1 h), C) DQB (20 µM, 1 h), or D) MβCD (5 mM, 1 h), further incubated with FFBCN1 (100 µM, 16 h), and subsequently incubated with complex **3** (20 µM, 4 h, λ_{ex} = 405 nm, and λ_{em} = 700 – 800 nm). Conditions for E to H are the same as A to D, except that the concentration of FFBCN1 was 200 µM.

(Photo)cytotoxicity Studies

The (photo)cytotoxicity of (1) the ruthenium(II) complexes, (2) FFBCN1, and (3) the combination of low or high concentrations of FFBCN1 + ruthenium(II) complexes was investigated with 3-(4,5-dimethylthiazol-2-yl)-2,5-diphenyltetrazolium bromide (MTT) assay (Table 3). The cellular uptake efficiencies of the complexes were also determined (Table S4). Complex **1** was noncytotoxic in the dark with an IC_{50} value > 300 µM. Complexes **2** and **3** exhibited higher dark cytotoxicity with IC_{50} values of 16.3 and 23.9 µM, respectively. The increased dark cytotoxicity of complexes **2** and **3** compared to complex **1** should result from their higher cellular uptake efficiencies (**2** > **3** > **1**) (Table S4), which is in accordance with the lipophilic character of the ligands: Ph_2-phen > biq > bpy. Treatment of HeLa cells with FFBCN1 only demonstrated that the BCN-peptide was noncytotoxic in the dark or upon irradiation (IC_{50} > 400 µM), and could accumulate bioorthogonal sites via EISA without any inherent (photo)cytotoxicity. Although TEM studies (Figure 7C) showed that treatment with FFBCN1 (100 µM) could induce the formation

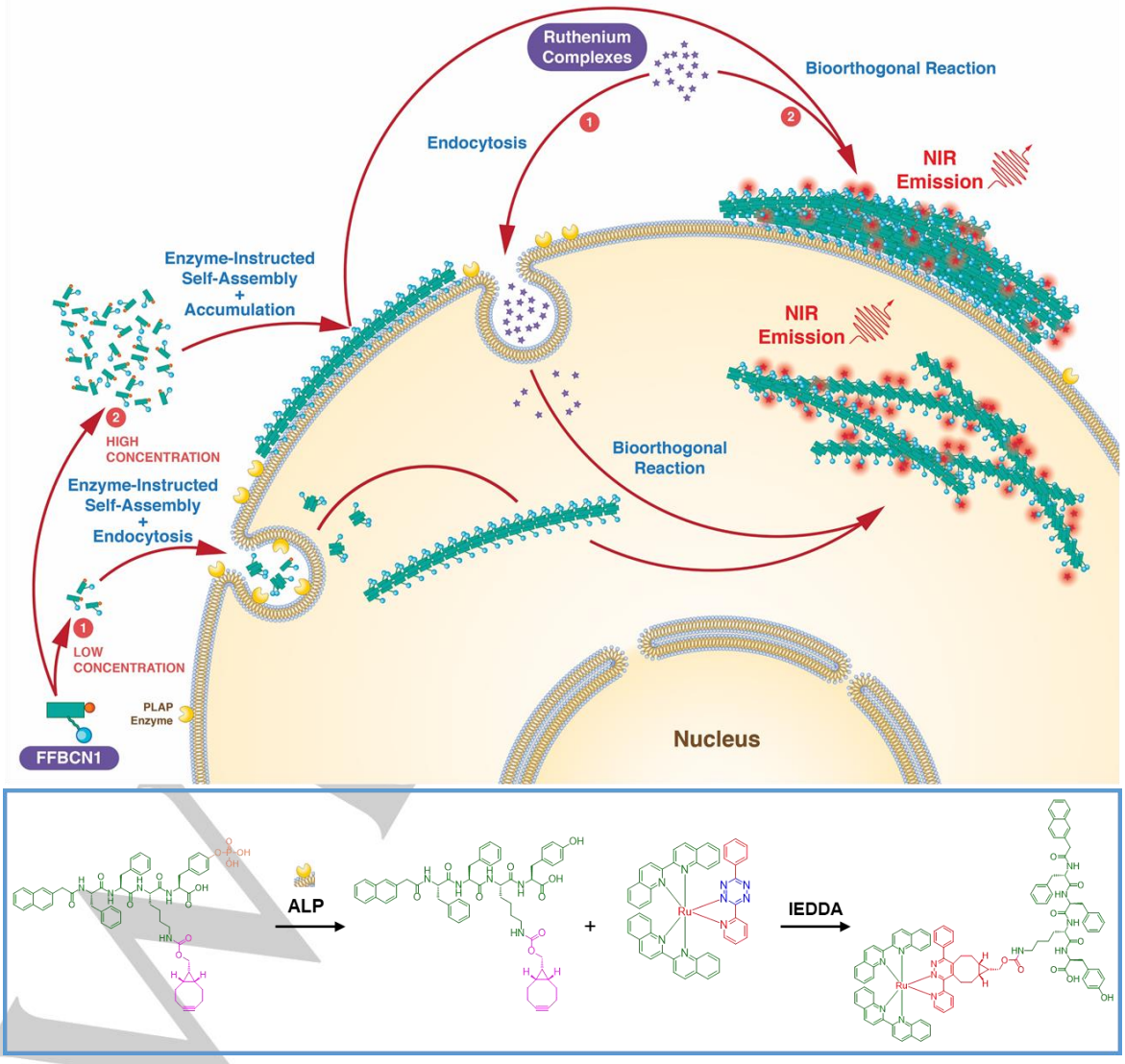

Figure 11. A combined enzymatic and bioorthogonal approach to specifically target: 1) intracellular or 2) extracellular regions of the cell. Enzyme-instructed self-assembly selectively accumulates bioorthogonal sites in cancer cells based on concentration-dependent dosage. Afterward, inert photosensitizers are directed to the accumulated bioorthogonal triggers and specifically activated through IEDDA reactions to generate NIR-emissive photosensitizers.

Table 3. (Photo)cytotoxicity of complexes **1** – **3** toward HeLa and HEK293 cells in the dark and upon irradiation at 450 nm (15.5 mW cm^{-2}, 15 min). PI is the ratio of $IC_{50,dark}/IC_{50,light}$.

		[FFBCN1] = 0 μM			[FFBCN1] = 100 μM			[FFBCN1] = 200 μM		
	Complex	$IC_{50,dark}$ [μM]	$IC_{50,light}$ [μM]	PI	$IC_{50,dark}$ [μM]	$IC_{50,light}$ [μM]	PI	$IC_{50,dark}$ [μM]	$IC_{50,light}$ [μM]	PI
HeLa	**1**	> 300	> 300	—[a]	> 300	3.4 ± 0.7	88.2	> 300	7.6 ± 2.5	39.5
	2	16.3 ± 3.7	0.3 ± 0.1	54.3	35.2 ± 6.0	0.35 ± 0.3	100.6	56.8 ± 0.7	1.6 ± 0.1	35.5
	3	23.9 ± 2.2	3.7 ± 1.7	6.5	44.4 ± 0.7	2.4 ± 0.2	18.5	61.1 ± 1.3	3.8 ± 0.5	16.1
HEK293	**1**	> 300	> 300	—[a]	> 300	> 300	—[a]	> 300	> 300	—[a]
	2	19.8 ± 1.8	0.5 ± 0.1	39.6	8.6 ± 1.3	1.1 ± 0.3	7.8	8.7 ± 0.8	0.8 ± 0.1	10.9
	3	90.3 ± 6.7	10.7 ± 1.7	8.4	30.6 ± 2.6	5.8 ± 1.0	5.3	27.6 ± 1.3	5.0 ± 0.5	5.5

[a] Could not be determined with accuracy.

of large holes in the cytoplasmic region of HeLa cells, it is likely that these holes merely weaken the cancer cells and may not be sufficient to reduce the cell viability. Upon photoirradiation, complex **1** showed no photocytotoxicity toward HeLa cells, with an IC_{50} value > 300 μM (Table 3, upper). Conversely, complexes **2** and **3** displayed moderate photocytotoxic activity with IC_{50} values of 0.3 and 3.7 μM and photocytotoxicity index (PI) values of 54.3 and 6.5, respectively. In the combined treatment condition, HeLa cells were pretreated with FFBCN1 (100 or 200 μM), washed with PBS, treated with complexes **1** – **3**, and kept in the dark or irradiated. Complex **1** remained noncytotoxic in the dark when pretreated with low or high concentrations of FFBCN1 (IC_{50} > 300 μM). Interestingly, the dark cytotoxicity decreased for both complexes **2** (IC_{50} = 35.2 and 56.8 μM at low and high [FFBCN1]) and **3** (IC_{50} = 44.4 and 61.1 μM at low and high [FFBCN1]). This may result from the transformation of the tetrazine unit to a pyridazine moiety, and the reduced interactions of the complexes with biomolecules inside the cells. Notably, complex **1** revealed significantly higher photocytotoxic activity at low [FFBCN1] (IC_{50} = 3.4 μM) than at high [FFBCN1] (IC_{50} = 7.6 μM) by *ca.* 2-fold. This trend was also observed when the HeLa cells were treated with complex **2** (IC_{50} = 0.35 and 1.6 μM at low and high [FFBCN1]) or complex **3** (IC_{50} = 2.4 and 3.8 μM at low and high [FFBCN1]). In the low FFBCN1 condition, the larger photocytotoxicity could be due to the difference in localization, as shown in Figure 9. The generation of $^1O_2$ species typically has limited lifetimes (< 3 μs) and diffusive distances (< 0.3 μm) in biological environments,[29] further highlighting that localization and subcellular organelle targeting is a highly important parameter to develop effective PDT agents with controlled photocytotoxicity. The low condition should lead to the generation of $^1O_2$ in the intracellular region of the cell with disruptive effects to the mitochondria. In contrast, the $^1O_2$ generated by the ruthenium(II) complexes pretreated with a high concentration of FFBCN1 are predominately localized on the membrane, and may diffuse readily into the extracellular space, leading to reduced photocytotoxicity. To validate that the low condition would lead to the intracellular generation of $^1O_2$ and disruption to mitochondria, CM-H_2DCFDA and rhodamine 123 (R123) were utilized to monitor ROS generation and mitochondria membrane potential (MMP), respectively. Strong emission intensity for the CM-H_2DCFDA probe was observed for the combined treatment of FFBCN1 (100 μM), complex **3**, and light irradiation (Figure S11). Pretreatment of HeLa cells with NaN_3, a $^1O_2$ scavenger,[30] effectively diminished the emission of the combined treatment, indicating that $^1O_2$ was generated intracellularly. Additionally, MMP studies demonstrated that the combined treatment induced complete disruption of MMP in HeLa cells (Figure S12).

We also assessed the cancer selectivity of this strategy against HEK293 cells. Treatment of HEK293 cells with FFBCN1 showed that the BCN-peptide was innocuous in the dark or upon irradiation (IC_{50} > 400 μM). Complexes **1** – **3** displayed reduced cytotoxicity and photocytotoxic activity in HEK293 cells (Table 3, lower), which could be promising to lessen adverse effects on normal cells. Complex **1** was shown to exhibit exceptional selectivity when pretreated with low or high concentrations of FFBCN1 with no harmful effects toward HEK293 cells (IC_{50} > 300 μM at low and high [FFBCN1]). Interestingly, the (photo)cytotoxicity of complex **2** pretreated with low or high concentrations of FFBCN1 showed very similar IC_{50} values regardless of the concentration of FFBCN1 ($IC_{50,dark}$ = 8.6 and 8.7 μM at low and high [FFBCN1], respectively; $IC_{50,light}$ = 1.1 and 0.8 μM at low and high [FFBCN1], respectively). This trend was also observed for complex **3** ($IC_{50,dark}$ = 30.6 and 27.6 μM at low and high [FFBCN1], respectively; $IC_{50,light}$ = 5.8 and 5.0 μM at low and high [FFBCN1], respectively). Overall, the combined treatment of FFBCN1 and complexes **1** – **3** showed reduced photocytotoxicity in normal HEK293 cells and good selectivity toward cancer cells.

Although the PI values obtained for the ruthenium(II) complexes in HeLa cells are modest compared to other ruthenium(II) photosensitizers and photoactivated chemotherapy agents (Table S5), these results highlight that the combination of EISA and bioorthogonal reactions could selectively accumulate in cancer cells and elicit enhanced photocytotoxic activity.

Conclusion

A self-assembling motif and ruthenium(II) complexes were developed as a synergistic EISA and bioorthogonal strategy for NIR imaging of intracellular and extracellular regions and

controllable activation of the ruthenium(II)-based photosensitizers. The incorporation of a bioorthogonal reporter group on an EISA unit improves the self-assembling capabilities of the resulting conjugate without interfering with the dephosphorylation activity of ALP enzymes. Adoption of a combined EISA and bioorthogonal strategy facilitates the formation of larger supramolecular assemblies and greater phosphorogenic response and lifetime extension of the ruthenium(II) complexes from the local hydrophobic environment offered by the assemblies. The present work showed that the accumulation of bioorthogonal EISA assemblies was achieved extracellularly and intracellularly, and the localization of the ruthenium(II) complexes would depend on the formed supramolecular assemblies. The dark cytotoxicity of the ruthenium(II) complexes could be reduced upon IEDDA with the EISA assemblies, and the PI significantly increased. This property could reduce the dark cytotoxicity of bioorthogonal-based photosensitizers, but improve the photocytotoxic activity of these PDT agents. Additionally, the photocytotoxicity was shown to be more effective in intracellular regions than extracellular due to the effective generation of $^1O_2$ proximal to subcellular organelles rather than diffusion across the cell membrane or extracellular space. The two-step approach described herein could be employed to track different extracellular and intracellular events and serve as an alternative therapeutic approach. The versatility of this strategy allows the interchanging of bioorthogonal diagnostic or therapeutic reagents to target other overexpressed cancer markers.

Acknowledgements

We thank the Hong Kong Research Grants Council (Project Nos. CityU 11302820, CityU 11301121, CityU 11317022, T42-103/16-N, C6014-20W, and C7075-21GF) and the Hong Kong Research Grants Council, National Natural Science Foundation of China (Project No. N_CityU104/21) for financial support. We also thank the funding support from “Laboratory for Synthetic Chemistry and Chemical Biology” under the Health@InnoHK Program launched by Innovation and Technology Commission, The Government of Hong Kong SAR, P. R. China. J. S. acknowledges the receipt of a Postgraduate Studentship administered by City University of Hong Kong.

Conflict of Interest

The authors declare no conflict of interest.

Data Availability Statement

The data that supports the findings of this study are available in the Supporting Information of this article.

Keywords: Bioorthogonal • Enzyme-Instructed Self-Assembly • Imaging Agents • Photosensitizers • Ruthenium

[1] a) L. K. Mckenzie, H. E. Bryant, J. A. Weinstein, *Coord. Chem. Rev.* **2019**, *379*, 2; b) C. Imberti, P. Zhang, H. Huang, P. J. Sadler, *Angew. Chem. Int. Ed.* **2020**, *59*, 61.

[2] a) S. Monro, K. L. Colón, H. Yin, J. Roque, P. Konda, S. Gujar, R. P. Thummel, L. Lilge, C. G. Cameron, S. A. McFarland, *Chem. Rev.* **2019**, *119*, 797; b) R. Baskaran, J. Lee, S.-G. Yang, *Biomater. Res.* **2018**, *22*, 25; c) H. Patel, R. Mick, J. Finlay, T. C. Zhu, E. Rickter, K. A. Cengel, B. Malkowicz, S. M. Hahn, T. M. Busch, *Clin. Cancer Res.* **2008**, *14*, 4869; d) A. Kawczyk-Krupka, K. Wawrzyniec, S. K. Musiol, M. Potempa, A. M. Bugaj, A. Sieroń, *Photodiagnosis Photodyn. Ther.* **2015**, *12*, 567.

[3] a) X. Li, S. Lee, J. Yoon, *Chem. Soc. Rev.* **2018**, *47*, 1174; b) H. J. Forman, H. Zhang, A. Rinna, *Mol. Asp. Med.* **2009**, *30*, 1.

[4] a) H. Wang, Z. Feng, B. Xu, *Chem. Soc. Rev.* **2017**, *46*, 2421; b) G. Li, X. Hu, P. Nie, D. Mang, S. Jiao, S. Zhang, S. R. Roy, S. Yukawa, S. Asahina, H. Sugasawa, W. Cortes, Z. Zhou, Y. Zhang, *Nano Lett.* **2021**, *21*, 747; c) H. He, W. Tan, J. Guo, M. Yi, A. N. Shy, B. Xu, *Chem. Rev.* **2020**, *120*, 9994.

[5] S. M. Shaban, S. B. Jo, E. Hafez, J. H. Cho, D.-H. Kim, *Coord. Chem. Rev.* **2022**, *465*, 214567.

[6] H. Wang, Z. Feng, Y. Qin, J. Wang, B. Xu, *Angew. Chem. Int. Ed.* **2018**, *57*, 4931; b) Z. Feng, H. Wang, B. Xu, *J. Am. Chem. Soc.* **2018**, *140*, 16433; c) H. He, S. Liu, D. Wu, B. Xu, *Angew. Chem. Int. Ed.* **2020**, *59*, 16445.

[7] G. Li, T. Sasaki, S. Asahina, M. C. Roy, T. Mochizuki, K. Koizumi, Y. Zhang, *Chem* **2017**, *2*, 283.

[8] a) J. Zhou, X. Du, X. Chen, J. Wang, N. Zhou, D. Wu, B. Xu, *J. Am. Chem. Soc.* **2018**, *140*, 2301; b) Z. Feng, H. Wang, S. Wang, Q. Zhang, X. Zhang, A. A. Rodal, B. Xu, *J. Am. Chem. Soc.* **2018**, *140*, 9566; c) Z. Feng, X. Han, H. Wang, T. Tang, B. Xu, *Chem* **2019**, *5*, 2442; d) H. Wang, Z. Feng, B. Xu, *Angew. Chem. Int. Ed.* **2019**, *58*, 5567; e) S. Liu, Q. Zhang, A. N. Shy, M. Yi, H. He, S. Lu, B. Xu, *J. Am. Chem. Soc.* **2021**, *143*, 15852; f) W. Tan, Q. Zhang, J. Wang, M. Yi, H. He, B. Xu, *Angew. Chem. Int. Ed.* **2021**, *60*, 12796; g) W. Tan, Q. Zhang, M. C. Quiñones-Frías, A. Y. Hsu, Y. Zhang, A. Rodal, P. Hong, H. R. Luo, B. Xu, *J. Am. Chem. Soc.* **2022**, *144*, 6709; h) M. Yi, F. Wang, W. Tan, J.-T. Hsieh, E. H. Egelman, B. Xu, *J. Am. Chem. Soc.* **2022**, *144*, 13055.

[9] a) Q. Yao, F. Lin, X. Fan, Y. Wang, Y. Liu, Z. Liu, X. Jiang, P. R. Chen, Y. Gao, *Nat. Commun.* **2018**, *9*, 5032; b) Q. Yao, S. Gao, C. Wu, T. Lin, Y. Gao, *Biomaterials* **2021**, *277*, 121119; c) Y. Zhao, Q. Yao, J. Chen, R. Zhang, J. Song, Y. Gao, *Biomater. Sci.* **2022**, *10*, 5662.

[10] a) Y. Zhang, B. Zhang, Y. Kuang, Y. Gao, J. Shi, X. X. Zhang, B. Xu, *J. Am. Chem. Soc.* **2013**, *135*, 5008; b) Y. Zheng, G. Li, Y. Zhang, *ChemNanoMet* **2016**, *2*, 364.

[11] a) P. K.-K. Leung, K. K.-W. Lo, *Chem. Commun.* **2020**, *56*, 6074; b) P. K.-K. Leung, L. C.-C. Lee, H. H.-Y. Yeung, K.-W. Io, K. K.-W. Lo, *Chem. Commun.* **2021**, *57*, 4914.

[12] a) S. P.-Y. Li, A. M.-H. Yip, H.-W. Liu, K. K.-W. Lo, *Biomaterials* **2016**, *103*, 305; b) L. C.-C. Lee, J. C.-W. Lau, H.-W. Liu, K. K.-W. Lo, *Angew. Chem. Int. Ed.* **2016**, *55*, 1046.

[13] a) T. S.-M. Tang, H.-W. Liu, K. K.-W. Lo, *Chem. Commun.* **2017**, *53*, 3299; b) A. M.-H. Yip, C. K.-H. Lai, K. S.-M. Yiu, K. K.-W. Lo, *Angew. Chem. Int. Ed.* **2022**, *61*, e202116078.

[14] a) A. Juris, V. Balzani, F. Barigelletti, S. Campagna, P. Belser, A. von Zelewsky, *Coord. Chem. Rev.* **1988**, *84*, 85; b) T. S.-M. Tang, A. M.-H. Yip, K. Y. Zhang, H.-W. Liu, P. L. Wu, K. F. Li, K. W. Cheah, K. K.-W. Lo, *Chem. Eur. J.* **2015**, *21*, 10729; c) T. S.-M. Tang, H.-W. Liu, K. K.-W. Lo, *Chem. Eur. J.* **2016**, *22*, 9649; d) C. T.-S. Lau, C. Chan, K. Y. Zhang, V. A. L. Roy, K. K.-W. Lo, *Eur. J. Inorg. Chem.* **2017**, *2017*, 5288; e) J. Karges, S. Kuang, F. Maschietto, O. Blacque, I. Ciofini, H. Chao, G. Gasser, *Nat. Commun.* **2020**, *11*, 3262.

[15] a) F. Barigelletti, P. Belser, A. von Zelewsky, A. Juris, V. Balzani, *J. Phys. Chem.* **1985**, *89*, 3680; b) D. Cullinane, K. S. Gkika, A. Byrne, T. E. Keyes, *J. Inorg. Biochem.* **2020**, *207*, 111032.

[16] R. J. Watts, G. A. Crosby, *J. Am. Chem. Soc.* **1972**, *94*, 2606.

[17] C. Müller, P. Wintergerst, S. S. Nair, N. Meitinger, S. Rau, B. Dietzek-Ivanšić, *J. Photochem. Photobiol.* **2022**, *11*, 100130.

[18] R. Rossin, P. R. Verkerk, S. M. van den Bosch, R. C. M. Vulders, I. Verel, J. Lub, M. S. Robillard, *Angew. Chem. Int. Ed.* **2010**, *49*, 3375.

[19] a) Y. Gao, Y. Kuang, Z.-F. Guo, Z. Guo, I. J. Krauss, B. Xu, *J. Am. Chem. Soc.* **2009**, *131*, 13576; b) A. N. Shy, B. J. Kim, B. Xu, *Matter* **2019**, *1*, 1127.

[20] J. Zhou, X. Du, Y. Gao, J. Shi, B. Xu, *J. Am. Chem. Soc.* **2014**, *136*, 2970.

[21] J. Zhou, X. Du, C. Berciu, H. He, J. Shi, D. Nicastro, B. Xu, *Chem* **2016**, *1*, 246.

[22] A. Müller, C. Klöppel, M. Smith-Valentine J. V. Houten, M. Simon, *Biochim. Biophys. Acta Biomembr.* **2012**, *1818*, 117.

[23] R. Dahl, E. A. Sergienko, Y. Su, Y. S. Mostofi, L. Yang, A. M. Simao, S. Narisawa, B. Brown, A. Mangravita-Novo, M. Vicchiarelli, L. H. Smith, W. C. O'Neill, J. L. Millán, N. D. P. Cosford, *J. Med. Chem.* **2009**, *52*, 6919.

[24] a) D. E. Saslowsky, J. Lawrence, X. Ren, D. A. Brown, R. M. Henderson, J. M. Edwardson, *J. Biol. Chem.* **2002**, *277*, 26966; b) A. H. van der Luit, M. Budde, M. Verheij, W. J. van Blitterswijk, *Biochem. J.* **2003**, *374*, 747.

[25] S. K. Rodal, G. Skretting, Ø. Garred, F. Vilhardt, B. van Deurs, K. Sandvig, *Mol. Biol. Cell* **1999**, *10*, 961.

[26] a) A. R. Hirst, S. Roy, M. Arora, A. K. Das, N. Hodson, P. Murray, S. Marshall, N. Javid, J. Sefcik, J. Boekhoven, J. H. van Esch, S. Santabarbara, N. T. Hunt, R. V. Ulijin, *Nat. Chem.* **2010**, *2*, 1089; b) J. Wang, K. Liu, R. Xing, X. Yan, *Chem. Soc. Rev.* **2016**, *45*, 5589; c) J. Zhou, X. Du, N. Yamagata, B. Xu, *J. Am. Chem. Soc.* **2016**, *138*, 3813; d) Z. Feng, H. Wang, X. Chen, B. Xu, *J. Am. Chem. Soc.* **2017**, *139*, 15377; e) Q. Yao, Z. Huang, D. Liu, J. Chen, Y. Gao, *Adv. Mater.* **2019**, *31*, 1804814; f) H. Wang, Z. Feng, B. Xu, *ChemBioChem* **2019**, *20*, 2442; g) J. Gao, J. Zhan, Z. Yang, *Adv. Mater.* **2020**, *32*, 1805798; h) J. Song, Q. Zhang, G. Li, Y. Zhang, *Langmuir* **2022**, *38*, 8733; i) F. Tian, M. Yang, Q. Yao, J. Song, J. He, X. Shi, Y. Gao, *Nano Today* **2022**, *47*, 101658.

[27] W. H. Fishman, N. R. Inglis, S. Green, C. L. Anstiss, N. K. Gosh, A. E. Reif, R. Rustigian, M. J. Krant, L. L. Stolbach, *Nature* **1968**, *219*, 697.

[28] S. Goldfischer, *J. Histochem. Cytochem.* **1982**, *30*, 717.

[29] E. Skovsen, J. W. Synder, J. D. C. Lambert, P. R. Ogilby, *J. Phys. Chem. B* **2005**, *109*, 8570.

[30] X. Ding, Q. Xu, F. Liu, P. Zhou, Y. Gu, J. Zeng, J. An, W. Dai, X. Li, *Cancer Lett.* **2004**, *216*, 43.

10.1002/anie.202303931

WILEY-VCH

RESEARCH ARTICLE

Entry for the Table of Contents

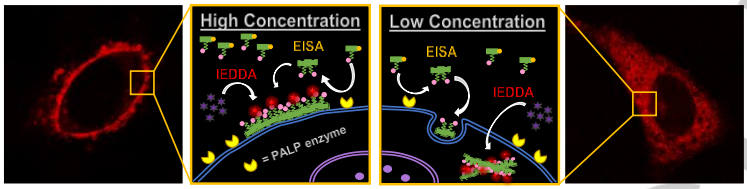

A concerted strategy involving enzyme-instructed self-assembly to target overexpressed alkaline phosphatases in cancer cells and bioorthogonal reactions for controllable extracellular and intracellular activation of Ru(II)-based imaging probes and photosensitizers are depicted. The emission enhancement, lifetime extension, and (photo)cytotoxicity extracellularly and intracellularly of the resulting Ru(II) supramolecular assemblies were explored.

Institute and/or researcher Twitter usernames: @bhkenlo